

p-Diamond, Si, GaN and InGaAs TeraFETs

Yuhui Zhang, *Student Member, IEEE*, and Michael S. Shur, *Life Fellow, IEEE*

Abstract—p-diamond field effect transistors (FETs) featuring large effective mass, long momentum relaxation time and high carrier mobility are a superb candidate for plasmonic terahertz (THz) applications. Previous studies have shown that p-diamond plasmonic THz FETs (TeraFETs) could operate in plasmonic resonant mode at a low frequency window of 200 to 600 GHz, thus showing promising potential for beyond 5G sub-THz applications. In this work, we explore the advantages of p-diamond transistors over n-diamond, Si, GaN and InGaAs TeraFETs and estimate the minimum mobility required for the resonant plasmons. Our numerical simulation shows that the p-diamond TeraFET has a relatively low minimum resonant mobility, and thus could enable resonant detection. The diamond response characteristics can be adjusted by changing operating temperature. A decrease of temperature from 300 K to 77 K improves the detection performance of TeraFETs. At both room temperature and 77 K, the p-diamond TeraFET presents a high detection sensitivity in a large dynamic range. When the channel length is reduced to 20 nm, the p-diamond TeraFET exhibits the highest DC response among all types of TeraFETs in a large frequency window.

Index Terms—P-diamond, Plasma wave electronics, TeraFET, THz detection, DC response.

I. INTRODUCTION

Recently, there has been a tremendous advance in the analysis and design of plasmonic terahertz (THz) semiconductor devices [1-6] due to the pressing demand of applications in various industrial fields. The fundamental theories of plasma-wave terahertz field-effect transistors (TeraFET) were developed in 1990s [7-9], later verified and supplemented by further experimental and analytical works [2, 3, 10, 11]. By now, THz imaging [12], sensing [13], communication [14] and optical pulse detection [6] are four mainstream applications of TeraFETs.

TeraFETs have been implemented in silicon [15], InGaAs [3], III-N [16], and graphene [17]. Recently, p-diamond has been proposed as another promising candidate for plasmonic THz applications [4]. Diamond is a wide bandgap material (~5.46 eV) and has a relatively high dielectric strength (~5 to 10 MV/cm) as well as a high thermal conductivity (about 23 W/cm·K) [4]. Those characteristics make diamond a very promising material for power and high temperature applications. Diamond can also be used for RF power device applications since it can withstand a large microwave signal [18]. In above applications, both delta [19, 20] and transfer

doping diamond devices [21, 22] operated at various temperatures.

Diamond has a high optical phonon energy and a large effective mass, resulting in a very large momentum relaxation time τ [4] making it easier to meet the plasmonic resonance condition $\omega_p\tau > 1$, where ω_p is the plasma frequency [7]. With a high momentum relaxation time, the plasmonic resonance can be achieved at a relatively low frequency. This makes diamond promising for plasmonic THz application in the 240 to 320 GHz range allocated for beyond 5G Wi-Fi communications. [13, 14]. Diamond FETs also have a relatively low ohmic contact resistance [4], which makes diamond even more advantageous for THz electronic applications.

Compared to n-diamond, p-diamond has a larger effective mass (0.63-2.1 according to various reports [4, 23, 24]) and a comparable maximum carrier mobility (as high as ~0.53 m²·V⁻¹·s⁻¹ [4, 25]). Therefore, here we focus on the characteristics of p-diamond as a TeraFET material.

II. BASIC EQUATIONS

We use one-dimensional hydrodynamic fluid model to trace the generation and propagation of plasma waves in gated plasmonic terahertz FETs (TeraFETs) implemented in p-diamond, n-diamond Si, GaN, and InGaAs, with feature sizes of 20 nm, 65 nm, and 130 nm at 300 K and 77 K. Table 1 lists the materials parameters used in the simulation. The mobilities used in our simulation are relatively large. The governing hydrodynamic model equations are [3, 11]

$$\frac{\partial n}{\partial t} + \nabla \cdot (n\mathbf{u}) = 0 \quad (1)$$

$$\frac{\partial \mathbf{u}}{\partial t} + (\mathbf{u} \cdot \nabla)\mathbf{u} + \frac{e}{m}\nabla U + \frac{\mathbf{u}}{\tau} - \nu\nabla^2\mathbf{u} = 0 \quad (2)$$

$$\begin{aligned} \frac{\partial \theta}{\partial t} + \nabla \cdot (\theta\mathbf{u}) - \frac{\chi}{C_v}\nabla^2\theta - \frac{mv}{2C_v}\left(\frac{\partial u_i}{\partial x_j} + \frac{\partial u_j}{\partial x_i} - \delta_{ij}\frac{\partial u_k}{\partial x_k}\right)^2 \\ = \frac{1}{C_v}\left(\frac{\partial W}{\partial t}\right)_c + \frac{m\mathbf{u}^2}{C_v\tau} \end{aligned} \quad (3)$$

Here n represents the carrier density, \mathbf{u} stands for the hydrodynamic velocity. The gate-to-channel potential U is defined as $U = U_0 - U_{ch}$ where U_0 is the gate bias above threshold and U_{ch} is the channel potential. The gradual channel approximation ($CU = en$, where C is the capacitance of barrier layer and is set to 0.56 $\mu\text{F}/\text{cm}^2$ [3]) is used in the simulation. τ

is the momentum relaxation time of carriers.

TABLE I
MATERIALS PARAMETERS USED IN THE SIMULATION

Material	m/m_0	Mobility (77 K)	Mobility (300 K)	Ref.
p-diamond	0.74	3.5	0.53	[4, 24, 25]
n-diamond	0.48	5	0.73	[4, 25, 26]
Si	0.19	2	1.45	[27-30]
GaN	0.24	3.1691	2	[30-32]
InGaAs	0.041	3.5	1.2	[6, 33, 34]

Note: m represents the effective mass of carriers, m_0 is the mass of free electrons. The unit of mobility is $\text{m}^2 \cdot \text{V}^{-1} \cdot \text{s}^{-1}$.

In the energy transport equation (3), $\theta = k_B T$ is the temperature in eV, χ is defined as $\chi = \kappa/n$ (κ is the heat conductivity) and has the same units as kinematic viscosity; C_V is the thermal capacitance; W is the total energy. $(\partial W/\partial t)_c$ represents the collision term of $\partial W/\partial t$, which can be expressed by $(\partial W/\partial t)_c = (\partial \Sigma/\partial t)_c - m\mu^2/\tau$, where $\Sigma = \theta^* F_1(\zeta)/F_0(\zeta)$ is the average internal energy, $\zeta = \ln(\exp(E_F/k_B T) - 1)$ is the chemical potential, $E_F = k_B T_F = \pi \hbar^2 n/m$ is the Fermi energy, and $F_k(\zeta)$ is the Fermi integral. Furthermore, ν is the viscosity of the 2DEG/2DHG, which is related to the carrier density and temperature. When the temperature T is much lower than the Fermi temperature T_F , χ and ν have the following expression [3, 6, 11]:

$$\nu(T) = \frac{2\hbar T_F^2}{\pi m T^2} \frac{1}{\ln(2T_F/T)} \quad (T \leq T_F) \quad (4)$$

$$\chi(T) = \frac{4\pi\hbar T_F}{3m T} \frac{1}{\ln(2T_F/T)} \quad (T \leq T_F) \quad (5)$$

Generally, the condition $T < T_F$ holds for relatively large gate bias U_0 (e.g. $U_0 > 2.3$ V for p-diamond TeraFETs), at which the viscosity and heat conductivity could be large. For small U_0 , $T > T_F$, and we use $\nu(T = T_F)$ and $\chi(T = T_F)$, which are constant values [3]. In this condition, the Navier-Stokes equation (2) effectively decouples from the heat transport equation (3).

The boundary conditions that we use are an open drain condition [3, 7]: $U(0, t) = U_0 + U_a(t)$ and $J(L, t) = 0$, where $U_a(t) = U_{\text{am}} \cos(\omega t)$ represents the AC voltage induced by the incoming THz radiation, J is the current flux density. The above equations were established and solved in COMSOL 5.4 [35] using the finite element method. More detailed introductions of the hydrodynamic model are given in [3] and [11].

In addition to the numerical modeling, we also use analytical theories to predict the DC response and compare it with modeling results. The analytical equations for DC response in TeraFETs were first established in [7] and were further modified for more detailed applications [3, 11, 36]. Here we follow the analytical equations derived in [7].

III. RESULTS AND DISCUSSION

A. Resonant versus non-resonant response

In sub-THz and THz plasmonic devices, the momentum relaxation time τ is a key parameter, as it determines the critical condition for the plasmonic resonance. Therefore, we first

compare the momentum relaxation time ($\tau = \mu m/e$) versus the mobility in different material systems, as shown in Fig. 1. Clearly, the p-diamond has the highest τ compared to other materials due to a high effective mass, and the value of τ varies between $\sim 10^{-14}$ s to $\sim 10^{-11}$ s as the mobility alters from 10^{-2} $\text{m}^2 \cdot \text{V}^{-1} \cdot \text{s}^{-1}$ to ~ 1 $\text{m}^2 \cdot \text{V}^{-1} \cdot \text{s}^{-1}$. In the case of highest τ , the resonance quality factor $\omega_p \tau$ could exceed unity at a very low frequency (as low as ~ 100 GHz or even smaller at cryogenic temperatures). Therefore, the frequency range for resonant detection in p-diamond TeraFETs could be much wider than devices made with stereotype materials, which is very promising for sub-THz communication applications.

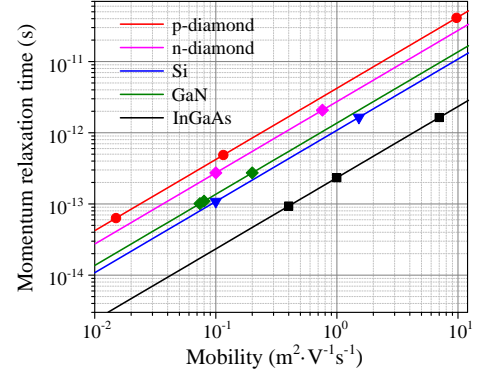


Fig. 1. Momentum relaxation time versus mobility for p-diamond, n-diamond, Si, InGaAs, GaN. Symbols represent measured values reported in: for p-diamond [4, 30], for n-diamond [4, 26], for Si [30, 37], for GaN [38, 39], for InGaAs [33, 40].

With a large effective mass, p-diamond TeraFETs could reach the plasma resonance condition $\omega_p \tau = 1$ at a relatively low frequency. It follows that at any given frequency, the critical τ (or critical mobility) required for resonant operation in p-diamond devices could also be low [4]. As reported previously, the minimal resonant mobility in TeraFETs can be evaluated by measuring the ultimate response time (τ_r) of the device and finding the mobility at which the minimum τ_r is reached [6, 41-43]. Here we also adopt this method. Fig. 2 shows the ultimate response time of TeraFETs made with different materials as a function of mobility. The τ_r values are calculated by feeding an ultra-short (5×10^{-14} s in this case) square-pulse signal to the source and evaluating the resulting voltage response [6]. In this figure, we also present the analytical response time curves for comparison. The analytical theory follows [6] and [3], in which the response was fit into an oscillating decay in the form of $\sum_{(n)} A_n \exp(\sigma_n t) f_n(x)$, where σ_n is obtained from the solution of linearized equations and is given by:

$$\sigma_n^\pm = \frac{1}{2} \left[-\left(\frac{1}{\tau} + \frac{\pi^2 \nu n^2}{4L^2} \right) \pm \sqrt{\left(\frac{1}{\tau} + \frac{\pi^2 \nu n^2}{4L^2} \right)^2 - \frac{\pi^2 s^2 n^2}{L^2}} \right] \quad (6)$$

$n = 1, 3, 5, \dots$

The response time of the periodic oscillation can be obtained from the first-order approximation, i.e. $\tau_r = 1/\text{Re}(|\sigma_1^+|)$.

As shown in Fig. 2(a1), for all materials, the response time initially decreases with μ , reaches a minimum, and then increases and gradually saturates. In the low mobility regime,

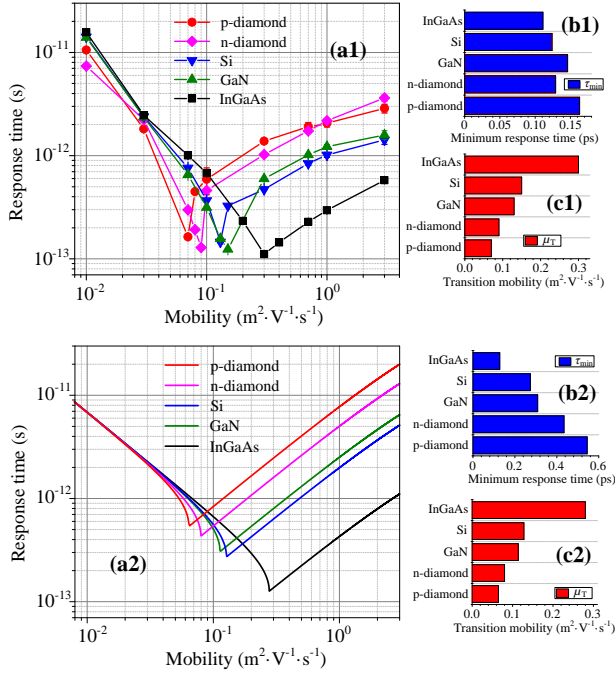


Fig. 2. Ultimate response times of TeraFETs made with 5 materials versus carrier mobility (a1), (a2), as well as their minimum response time (b1), (b2) and transition mobility (c1), (c2). (a1)-(c1) show the simulation data, and (a2)-(c2) present the analytical results. The gate voltage swing U_0 is set 0.1 V, the feature size L is 130 nm, the pulse width of incoming radiation is 5×10^{-14} s, under room temperature ($T = 300$ K).

the plasma waves are overdamped, and the voltage response is purely an exponential decay. The ultimate response time in this regime is on the order of $L/\mu U_0$ [6]. The high-mobility region corresponds to the region of resonant plasmonic operation. The minimum τ_r is reached at the transition mobility between two regimes [6, 41]. The general variation trend of τ_r shown in Fig. 2(a1) agrees with the analytical results in Fig. 2(a2). For transition mobility μ_T , as presented in Fig. 2(c1), p-diamond TeraFET has the lowest μ_T among 5 material systems, and the value of μ_T for p-diamond ($0.07 m^2 \cdot V^{-1} \cdot s^{-1}$) is much lower than those of GaN, Si and InGaAs transistors. It is also observed that those simulation values of μ_T conform well to the analytical data shown in Fig. 2(c2). Therefore, the plasmonic resonance is easier to be induced in the p-diamond TeraFET. This could be a huge advantage for p-diamond over other materials in making TeraFETs, since the realization of high carrier mobility could require substantial efforts.

In addition, it is also interesting to investigate the variation of ultimate response time and minimum resonant mobility with the channel length L . The results are presented in Fig. 3. As shown in Fig. 3(a), as L alters, the transition mobility and minimum τ_r reduces with decreasing L . This suggests that small-feature-size TeraFETs could be advantageous over those with large feature sizes. Fig. 3(b) presents the minimum mobility required for resonant plasmonic operation versus the feature size in p-diamond TeraFET. As seen, the critical mobility decreases almost linearly with the reduction of channel length. According to previous theoretical analyses, the transition mobility μ_T is on the order of $(eL/\pi ms)/(1-\pi v/4Ls)$, and the corresponding analytical curve is also given in Fig. 3(b).

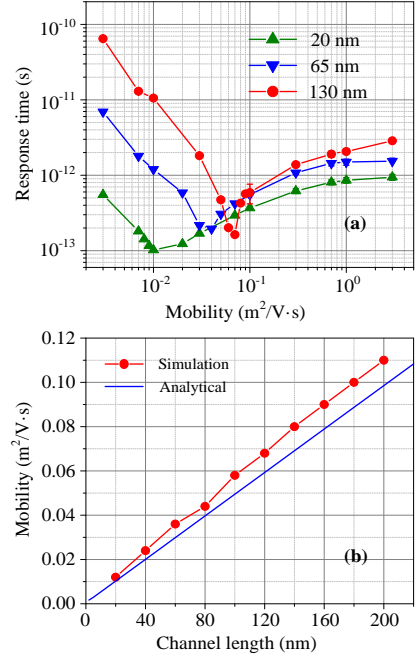


Fig. 3. Ultimate response time of the p-diamond TeraFET as a function of carrier mobility under 3 different channel lengths (a), as well as the transition mobility versus channel length for the same FET (b). The gate voltage swing U_0 is set 0.1 V and the pulse width of incoming radiation is 5×10^{-14} s, under room temperature.

Obviously, the analytical curve exhibits a linear feature. This is because the contribution of term $(1-\pi v/4Ls)$ is negligible in this case and thus the analytical value of μ_T is very close to $L e/\pi m s$, which has a linear dependence to L . Moreover, the simulation values are in good agreement with the theoretical results. The conformity between simulation and analytical results enables us to predict the minimum resonant mobility with the analytical equations obtained previously.

B. General frequency-dependent and bias dependent profiles

The above discussion shows that p-diamond TeraFETs have relatively high momentum relaxation times and low minimum resonant frequencies, therefore promising for plasmonic THz applications. Now we further discuss the characteristics of p-diamond TeraFETs from the perspective of DC voltage response. Fig. 4 presents the normalized DC voltage response versus gate bias for 5 types of plasmonic FETs under $T = 300$ K, $L = 130$ nm. Both analytical curves (solid lines) and simulation values (scatters) are depicted in this figure. The analytical DC source-to-drain voltage response is proportional to the power of incoming AC small signal [7]:

$$\frac{dU}{U_0} = \frac{1}{4} \frac{U_{am}^2}{U_0^2} f(\omega) \quad (7)$$

where U_{am} is the amplitude of incoming AC signal, $f(\omega)$ is a frequency dependent function and is always positive. Besides, the normalization of dU is performed as $R = dU \cdot U_0 / U_{am}^2$.

As shown in Fig. 4(a), at 300 K when the viscosity is relatively low, the simulation data show very good match with their corresponding analytical curves in p-diamond, n-diamond, Si and GaN cases. For the case of InGaAs, a significant discrepancy between simulation and analytical results is

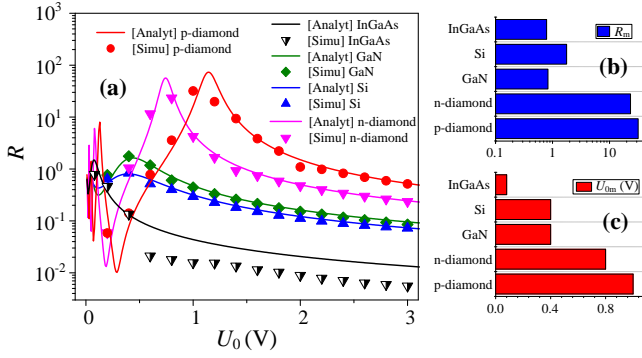


Fig. 4. Normalized response of different TeraFETs versus the gate bias U_0 (a), along with the amplitudes (b) and positions (c) of peak response. The frequency and amplitude of incoming small signal are set 1 THz and 0.5 mV, respectively. The channel length $L = 130$ nm, under room temperature.

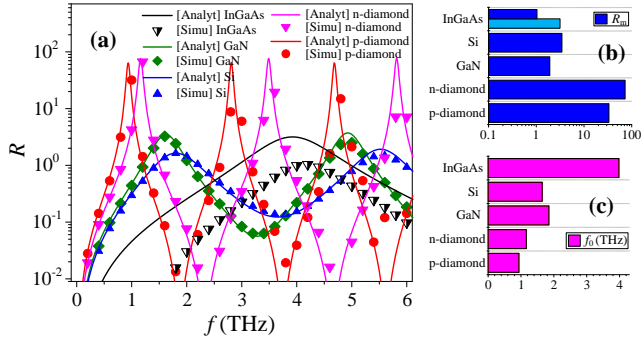


Fig. 5. Normalized response of different TeraFETs versus frequency f (a), along with the amplitudes of peak response (R_m) (b) and the values of fundamental frequency ($f_0 = s/4L$, where $s = (eU_0/m)^{0.5}$ is the plasma velocity) (c). The cyan bar in (b) presents the R_m in analytical curve. The frequency and amplitude of incoming small signal is 1 THz and 0.5 mV, respectively. The channel length $L = 130$ nm, under room temperature.

observed at $U_0 \geq 0.6$ V. Note that with a small effective mass, the viscosity of InGaAs could be remarkable even at room temperature (e.g. $\nu = 179.4 \text{ cm}^2 \cdot \text{V}^{-1} \text{ s}^{-1}$ at $U_0 = 0.6$ V). Therefore, this mismatch between simulation and theory is likely attributed by the high viscosity of InGaAs. Furthermore, it can be seen from Fig. 4(b) that p-diamond TeraFET has the largest peak response, and it leads all TeraFETs in response when U_0 is above 1 V. This indicates that p-diamond detectors might be most advantages for high gate bias operation at room temperature. Besides, the position of resonant peak U_{0r} can be roughly obtained by the expression of fundamental resonant frequency, as given below:

$$n \cdot f_0 = n \cdot \frac{s}{4L} = \sqrt{\frac{n^2 e U_{0r-n}}{16mL^2}} = f \Rightarrow U_{0r-n} = \frac{16mL^2 f^2}{n^2 e} \quad (8)$$

where $n = 1, 3, 5 \dots$ is the odd harmonic ordinal. For a fixed f , a higher effective mass m would require a larger U_0 to meet the criterion for plasma resonance, and this is the reason why the peak of DC response curve moves rightward with increasing effective mass. The values of fundamental U_{0r} (i. e. $n = 1$) predicted by equation (8) for p-diamond, n-diamond, Si, GaN and InGaAs are 1.14 V, 0.74 V, 0.29 V, 0.37 V, 0.063 V, respectively, which in general agrees with the results of U_{0m} shown in Fig. 4(c). In addition, for p- and n-diamond TeraFETs, there are some other response peaks at relatively low gate bias region, corresponding to the higher order harmonics. Since the

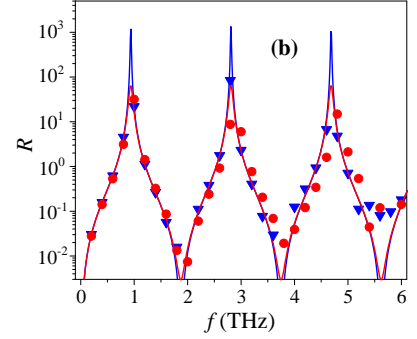
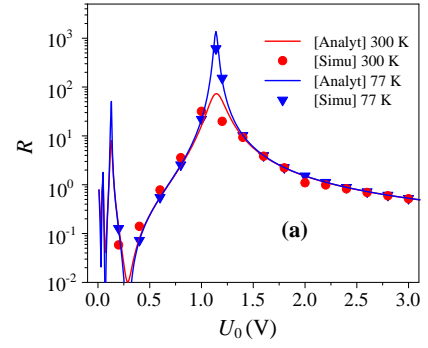


Fig. 6. Normalized response of the p-diamond TeraFET versus U_0 (a) and f (b) under typical mobilities at 3 temperatures. The f in (a) is 1 THz, and the U_0 in (b) is 1 V. The amplitude of incoming small signal is 0.5 mV. The channel length $L = 130$ nm.

value of R varies sharply in this region, a very low U_0 could be undesirable for THz detection.

Apart from the U_0 dependence, it is also important to study the frequency dependence of the DC response in different TeraFETs. With this in mind, we simulate the normalized voltage response versus the driving frequency presented in Fig. 5. As seen, the simulation data still conforms to the analytical curves for all types of TeraFETs except InGaAs. Also, the peaks of response curves are precisely located at the fundamental frequencies (see Fig. 5(c)) and their odds harmonics, indicating all the detectors operate at resonant regime. In this case, p-diamond TeraFET has the second highest peak response, which is much large than those of GaN, Si and InGaAs TeraFETs, as shown in Fig. 5(a) and Fig. 5(b). At low frequency ($f < 1$ THz), the response of p-diamond TeraFET is the highest among all devices. This suggests that p-diamond detector might be the most suitable one for sub-THz detection, which is of critical importance in technologies related to beyond-5G communications. Beyond 1 THz, the p-diamond TeraFET also yields the highest DC response in the vicinity of its harmonic peaks. Those features allow better performance for high sensitivity detection.

C. Temperature dependence of TeraFET detectors

To evaluate the performance of plasma wave TeraFET detectors at different temperatures, we explore the response profiles of TeraFETs at the cryogenic temperature (77 K) and compare the results with those at room temperature (300 K). It should be pointed out that in the present hydrodynamic model, the energy equation only considers the heat transfer process inside the device [2, 3, 11]. In cryogenic temperature simulation, this could lead to a significant self-heating by the THz signal (i.e. the temperature level in the channel rises with

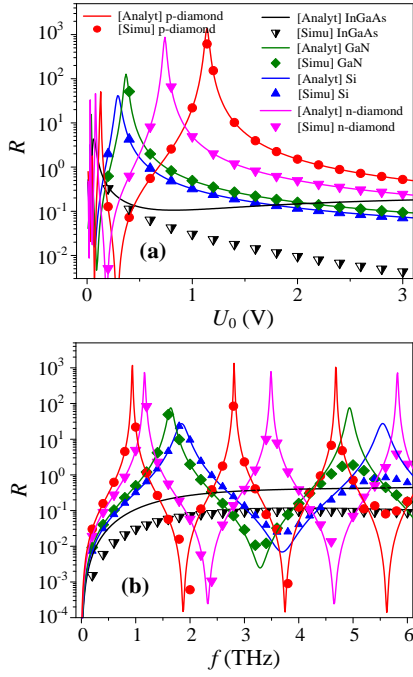


Fig. 7. Normalized response of different TeraFETs versus the gate bias U_0 (a) and frequency f (b) under $T = 77$ K. The amplitude of incoming small signal is set to be 0.5 mV. The channel length $L = 130$ nm. The f in (a) is fixed at 1 THz, and the U_0 in (b) is 1 V.

time and saturates above the environment temperature). While in the real system, this heating effect may not be as significant since the heat exchange between the channel and ambient environment is always crucial. In our simulation, we assume temperature equilibrium for $T = 77$ K throughout the simulation period.

Fig. 6 plots the normalized DC response of p-diamond TeraFET versus U_0 and f at 2 temperatures. As seen from Fig. 6(a), a significant elevation in peak response is achieved when the system temperature drops from 300 K to 77 K. This is mainly attributed to a substantial increase in carrier mobility as T decreases from 300 K to 77 K. Fig. 6(b) illustrates the normalized DC response of p-diamond TeraFET as a function of frequency at 3 temperatures. Analogous to Fig. 6(a), the peak response increases as the temperature decreases from 300 K to 77 K. Those results suggest that the detector sensitivity could be even enhanced when the temperature drops.

To further demonstrate the effects of temperature variation on the detection characteristics, the DC response properties of TeraFETs at cryogenic temperature for other 4 materials are studied. Fig. 7 presents the gate bias and frequency dependence of response profiles for 5 types of TeraFETs under $T = 77$ K. Fig. 7(a) shows the gate bias dependence characteristics similar to those at $T = 300$ K, except that the response peaks are elevated due to the rise of mobility. The simulation data still conform to the analytical curves for p-diamond, n-diamond, Si and GaN TeraFETs, as the viscosity in those cases are still not too large to cause the distortion. Also, p-diamond TeraFET still has the highest peak response, and leads the response at $U_0 \geq 1$ V. Fig. 7(b) shows the frequency dependence of response profile at 77 K. From this figure we also observe a similar response characteristics and enhanced peak values compared to the 300 K case. Based on those results, it is clear that a cryogenic detection at $T = 77$ K does not alter the general

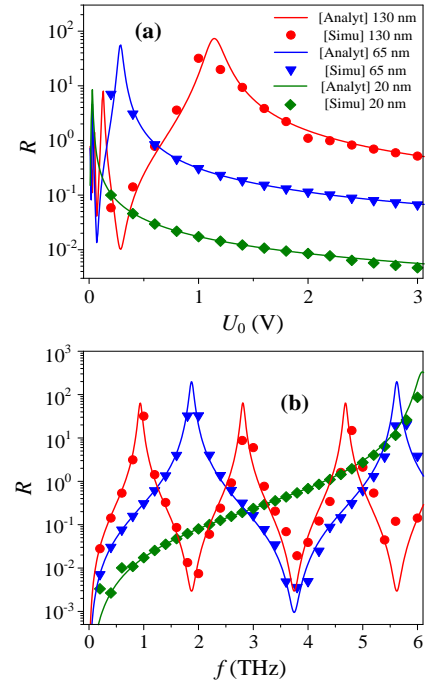


Fig. 8. Normalized response of the p-diamond TeraFET versus U_0 (a) and f (b) under typical mobilities at 3 channel lengths. The f in (a) is 1 THz, and the U_0 in (b) is 1 V. The amplitude of incoming small signal is 0.5 mV. The operating temperature is 300 K.

properties of THz detectors, while the detection sensitivity is improved. Also, the p-diamond TeraFET still presents a superior performance at 77 K. Besides, a slight mismatch between simulation and analytical results shows up at 77 K for diamond, Si and GaN TeraFETs, since the simulation curve appears to be more or less flattened at higher frequencies, while the theory predicts an undamped oscillation. This phenomenon is caused by the high viscosity effect [3, 7], and is consistent with the previous observation by Rudin *et al.* [3].

D. Channel length dependence of TeraFET detectors

In this section, we discuss the effect of device feature size on the detection properties of TeraFETs. Fig. 8 presents the DC response of p-diamond TeraFETs versus U_0 and f when the channel lengths are 130 nm, 65 nm and 20 nm at 300 K. As seen in Fig. 8(a), at $f = 1$ THz, the peak response and general response level decrease as L declines, indicating that a longer channel is preferred in this condition if a high responsivity is required. However, this rule may not hold under other frequencies. Fig. 8(b) illustrates the frequency spectrum of normalized response for p-diamond at 3 feature sizes. With the decrease of L , the maximum response rises. The rise of resonant response peak can be explained by the approximate expression of $f(\omega)$ in the vicinity of resonant peaks (i.e. $|\omega - n\omega_0| \ll \omega_0$, and $\omega\tau \gg 1$) [7]:

$$f(\omega) \approx 4\left(\frac{s\tau}{L}\right)^2 \frac{1}{4(\omega - n\omega_0)^2 \tau^2 + 1} \quad (9)$$

At resonant frequencies, $f(\omega) \sim 4(s\tau/L)^2$, which is inversely associated with L . Furthermore, the term $s\tau/L$ can also be used as the judgement for long/short devices. If $s\tau/L \ll 1$, the device can be regarded as a long device, and thus behaves like a broadband detector [7]. For L equals to 130 nm, 65 nm and 20 nm, the values of $s\tau/L$ are 8.367, 16.734 and 54.387,

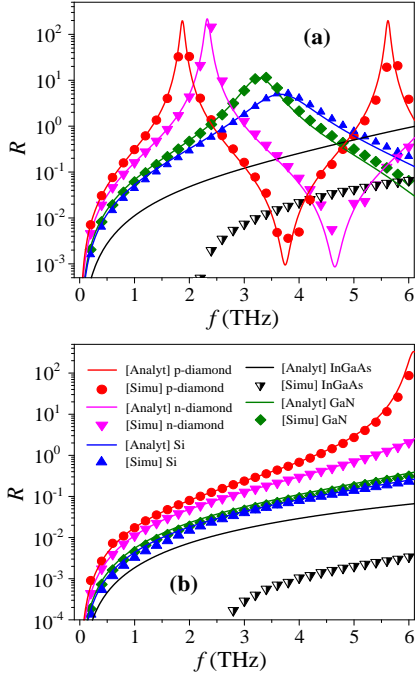


Fig. 9. Normalized response of the p-diamond TeraFET versus frequency under typical mobilities at channel lengths of 65 nm (a) and 20 nm (b). The DC gate bias U_0 is at 1 V, the amplitude of incoming small signal is 0.5 mV, and the operating temperature is 300 K.

respectively. Therefore, under the present mobility, the p-diamond TeraFET is always more qualified as a resonant detector when $L \leq 130$ nm. If we want to design a broadband detector, the channel length should be at least $s\tau = 1.09$ μm . One can also acquire a broadband detector by reducing the mobility of the p-diamond sample. If the carrier mobility in p-diamond is dropped to $0.015 \text{ m}^2 \cdot \text{V}^{-1} \cdot \text{s}^{-1}$ [4], the corresponding TeraFETs could serve as broadband detectors if L is no less than 30.8 nm..

To compare the L dependence of TeraFETs made with different materials, Fig. 9 plots the DC response of all 5 types of TeraFETs versus frequency under feature sizes of 65 nm and 20 nm at 300 K. As shown in Fig. 9(a), the relative response level of p-diamond TeraFET increases compared to the 130 nm case shown in Fig. 6(a). Furthermore, the frequency range within which the p-diamond device tops the response level expands. When L is reduced to 20 nm, this ‘‘p-diamond dominant’’ region expands further to at least $f = 6$ THz, as illustrated in Fig. 9(b). The extension of this frequency range is attributed to the increase of fundamental resonant frequency $f_0 = s/4L$ as L drops. Moreover, it is also noticed that the magnitude of the response shown in Fig. 9(b) is negatively correlated to the effective massive of the detector material. In fact, this rule is quite universal and holds in all the sub-THz regions shown in other figures (e.g. Fig. 5(a) and Fig. 7(b)). To explore the mechanism behind this rule, we consider the analytical response equation in this region. We first consider the low frequency region in which $\omega\tau \ll 1$ and $k_0' \approx k_0'' \approx (1/s) \cdot (\omega/2\tau)^{0.5} = k_0$, where k_0' and k_0'' are the real and imaginary part of wave vector for plasma wave propagation [3, 7]. In this region, we always have $k_0L \ll 1$, thus $\sin^2(k_0L) \approx 0$ and $\cos^2(k_0L) \approx 1$, then the expression of $f(\omega)$ becomes [7]:

$$f(\omega) = \frac{\sinh^2(k_0L) - \sin^2(k_0L)}{\sinh^2(k_0L) + \cos^2(k_0L)} \approx \frac{\sinh^2(k_0L)}{\sinh^2(k_0L) + 1} \quad (10)$$

$$= \frac{1}{1 + 1/\sinh^2(k_0L)}$$

Note that $k_0 \sim 1/s$ thus $k_0 \sim m^{0.5}$. With a larger effective mass, $\sin^2(k_0L)$ increases, leading to the increase of $f(\omega)$ and therefore the magnitude of DC response.

Now we further consider the region where $\omega\tau > 1$ and $\omega < \omega_0$. In this region, $k_0' \approx \omega/s$, $k_0'' \approx 1/2s\tau$. For the case of $L = 20$ nm, we have $k_0''L = L/2s\tau \ll 1$, thus $f(\omega)$ can be approximately expressed by [7]:

$$f(\omega) = \frac{3\sinh^2(k_0'L) + \sin^2(k_0'L)}{\sinh^2(k_0'L) + \cos^2(k_0'L)} \quad (11)$$

$$\approx \frac{\sin^2(k_0'L)}{\cos^2(k_0'L)} = \tan^2(k_0'L)$$

Since $k_0' \sim 1/s \sim m^{0.5}$, $f(\omega) = \tan^2(k_0'L)$ will be positively associated with the carrier effective mass. Therefore, in both high frequency and low frequency region, a higher carrier effective mass yields a higher DC response if the channel is short enough. Those discoveries suggest that p-diamond TeraFETs may be more advantageous as a high sensitivity detector under relatively small feature sizes.

IV. CONCLUSION

The hydrodynamic simulations show that the p-diamond TeraFETs can operate at the resonant mode within sub-terahertz frequency range, and have a relatively low critical resonant mobility, thus very suitable to be used as resonant detectors. Under the high gate bias and low frequency (sub-THz), the high mobility p-diamond TeraFETs have a higher DC voltage response compared to other TeraFETs. As the temperature drops from 300 K to 77 K, the general detection characteristics do not alter, while the amplitude of the response enhances, suggesting the feasibility of THz detection using plasmonic detectors at 77 K. At both room temperature and 77 K, p-diamond presents the largest peak response and leads all TeraFETs in DC response in a large dynamic range.

As the channel length reduces to 20 nm, the p-diamond TeraFET exhibits the highest DC response among all types of TeraFETs in a large frequency range. This indicates that the relative performance of p-diamond TeraFETs improves as the feature size scales down.

REFERENCES

- [1] V. Y. Kachorovskii and M. S. Shur, ‘‘Current-induced terahertz oscillations in plasmonic crystal,’’ *Applied Physics Letters*, vol. 100, no. 23, p. 232108, 2012.
- [2] S. Rudin, ‘‘Temperature dependence of the nonlinear plasma resonance in gated two-dimensional semiconductor conduction channels,’’ *Applied Physics Letters*, vol. 96, no. 25, p. 252101, 2010.
- [3] S. Rudin, G. Rupper, A. Gutin, and M. Shur, ‘‘Theory and measurement of plasmonic terahertz detector response to large signals,’’ *Journal of Applied Physics*, vol. 115, no. 6, p. 064503, 2014.
- [4] M. Shur, S. Rudin, G. Rupper, and T. Ivanov, ‘‘p-Diamond as candidate for plasmonic terahertz and far infrared applications,’’ *Applied Physics Letters*, vol. 113, no. 25, p. 253502, 2018.

- [5] I. V. Rozhansky, V. Y. Kachorovskii, and M. S. Shur, "Helicity-Driven Ratchet Effect Enhanced by Plasmons," *Physical Review Letters*, vol. 114, no. 24, p. 246601, Jun 19 2015.
- [6] S. Rudin, G. Rupper, and M. Shur, "Ultimate response time of high electron mobility transistors," *Journal of Applied Physics*, vol. 117, no. 17, p. 174502, 2015.
- [7] M. Dyakonov and M. Shur, "Detection, mixing, and frequency multiplication of terahertz radiation by two dimensional electronic fluid," *IEEE Transactions on Electron Devices*, vol. 43, no. 3, pp. 380-387, 1996.
- [8] M. I. Dyakonov and M. S. Shur, "Two dimensional electronic flute," *Applied Physics Letters*, vol. 67, no. 8, pp. 1137-1139, 1995.
- [9] M. Dyakonov and M. Shur, "Shallow water analogy for a ballistic field effect transistor: New mechanism of plasma wave generation by dc current," *Phys Rev Lett*, vol. 71, no. 15, pp. 2465-2468, Oct 11 1993.
- [10] J.-Q. Lü and M. S. Shur, "Terahertz detection by high-electron-mobility transistor: Enhancement by drain bias," *Applied Physics Letters*, vol. 78, no. 17, pp. 2587-2588, 2001.
- [11] G. Rupper, S. Rudin, and F. J. Crowne, "Effects of oblique wave propagation on the nonlinear plasma resonance in the two-dimensional channel of the Dyakonov-Shur detector," *Solid-State Electronics*, vol. 78, pp. 102-108, 2012.
- [12] D. B. Veksler, A. V. Muraviev, T. A. Elkhatib, K. N. Salama, and M. S. Shur, "Plasma wave FET for sub-wavelength THz imaging," presented at the International Semiconductor Device Research Symposium, 12-14 Dec., 2007.
- [13] T. George, A. K. Dutta, M. S. Islam, and M. S. Shur, "Plasmonic detectors and sources for THz communication and sensing," in *Proceedings of SPIE*, 2018, vol. 10639, pp. 1-10: SPIE.
- [14] S. Blin, F. Teppe, L. Tohme, S. Hisatake, K. Arakawa, P. Nouvel, D. Coquillat, A. Penarier, J. Torres, L. Varani, W. Knap, and T. Nagatsuma, "Plasma-Wave Detectors for Terahertz Wireless Communication," *IEEE Electron Device Letters*, vol. 33, no. 10, pp. 1354-1356, 2012.
- [15] W. Stillman, D. Veksler, T. A. Elkhatib, K. Salama, F. Guarin, and M. S. Shur, "Sub-terahertz testing of silicon MOSFET," *Electronics Letters*, vol. 44, no. 22, pp. 1325-1326, 2008.
- [16] W. Knap, D. Coquillat, N. Dyakonova, F. Teppe, O. Klimenko, H. Videlier, S. Nadar, J. Łusakowski, G. Valusis, F. Schuster, B. Giffard, T. Skotnicki, C. Gaquière, and A. El Fatimy, "Plasma excitations in field effect transistors for terahertz detection and emission," *Comptes Rendus Physique*, vol. 11, no. 7-8, pp. 433-443, 2010.
- [17] L. Vicarelli, M. S. Vitiello, D. Coquillat, A. Lombardo, A. C. Ferrari, W. Knap, M. Polini, V. Pellegrini, and A. Tredicucci, "Graphene field-effect transistors as room-temperature terahertz detectors," *Nat Mater*, vol. 11, no. 10, pp. 865-871, Oct 2012.
- [18] Y. Gurbuz, O. Esame, I. Tekin, W. P. Kang, and J. L. Davidson, "Diamond semiconductor technology for RF device applications," *Solid-State Electronics*, vol. 49, no. 7, pp. 1055-1070, 2005.
- [19] R. S. Balmer, I. Friel, S. M. Woollard, C. J. Wort, G. A. Scarsbrook, S. E. Coe, H. El-Hajj, A. Kaiser, A. Denisenko, E. Kohn, and J. Isberg, "Unlocking diamond's potential as an electronic material," *Philos Trans A Math Phys Eng Sci*, vol. 366, no. 1863, pp. 251-265, Jan 28 2008.
- [20] A. Aleksov, A. Vescan, M. Kunze, P. Gluche, W. Ebert, E. Kohn, A. Bergmaier, and G. Dollinger, "Diamond junction FETs based on d-doped channels," *Diamond and Related Materials*, vol. 8, pp. 941-945, 1999.
- [21] C. E. Nebel, "Surface Conducting Diamond.pdf," *Science*, vol. 318, no. 5855, pp. 1391-1392, 2007.
- [22] F. Maier, M. Riedel, B. Mantel, J. Ristein, and L. Ley, "Origin of surface conductivity in diamond," *Physical Review Letters*, vol. 85, no. 16, pp. 3472-3475, Oct 16 2000.
- [23] E. Gheeraert, S. Koizumi, T. Teraji, H. Kanda, and M. Nesládek, "Electronic States of Boron and Phosphorus in Diamond," *Phys. Status Solidi A*, vol. 174, pp. 39-51, 1999.
- [24] N. Naka, K. Fukai, Y. Handa, and I. Akimoto, "Direct measurement via cyclotron resonance of the carrier effective masses in pristine diamond," *Physical Review B*, vol. 88, no. 3, p. 035205, 2013.
- [25] I. Akimoto, Y. Handa, K. Fukai, and N. Naka, "High carrier mobility in ultrapure diamond measured by time-resolved cyclotron resonance," *Applied Physics Letters*, vol. 105, no. 3, p. 032102, 2014.
- [26] I. Akimoto, N. Naka, and N. Tokuda, "Time-resolved cyclotron resonance on dislocation-free HPHT diamond," *Diamond and Related Materials*, vol. 63, pp. 38-42, 2016.
- [27] F. Stern, "Calculated Temperature Dependence of Mobility in Silicon Inversion Layers," *Physical Review Letters*, vol. 44, no. 22, pp. 1469-1472, 1980.
- [28] R. A. Street, J. Kakalios, and M. Hack, "Electron drift mobility in doped amorphous silicon," *Phys Rev B Condens Matter*, vol. 38, no. 8, pp. 5603-5609, Sep 15 1988.
- [29] P. P. Altermatt, A. Schenk, F. Geelhaar, and G. Heiser, "Reassessment of the intrinsic carrier density in crystalline silicon in view of band-gap narrowing," *Journal of Applied Physics*, vol. 93, no. 3, pp. 1598-1604, 2003.
- [30] I. V. Gorbenko, V. Y. Kachorovskii, and M. Shur, "Terahertz plasmonic detector controlled by phase asymmetry," *Opt Express*, vol. 27, no. 4, pp. 4004-4013, Feb 18 2019.
- [31] W. Knap, E. Borovitskaya, M. S. Shur, L. Hsu, W. Walukiewicz, E. Frayssinet, P. Lorenzini, N. Grandjean, C. Skierbiszewski, P. Prystawko, M. Leszczynski, and I. Grzegory, "Acoustic phonon scattering of two-dimensional electrons in GaN/AlGaN heterostructures," *Applied Physics Letters*, vol. 80, no. 7, pp. 1228-1230, 2002.
- [32] R. Gaska, M. S. Shur, A. D. Bykhovski, A. O. Orlov, and G. L. Snider, "Electron mobility in modulation-doped AlGaIn-GaN heterostructures," *Applied Physics Letters*, vol. 74, no. 2, pp. 287-289, 1999.
- [33] J. James D. OLIVER, L. F. EASTMAN, P. D. KIRCHNER, and W. J. SCHAFF, "Electrical characterization and alloy scattering measurements of LPE GaIn_{1-x}As_xInP for high frequency device applications," *J. Cryst. Growth*, vol. 54, no. 1, pp. 64-68, 1981.
- [34] M. Levinshtein, S. Rumyantsev, and M. Shur, *Handbook Series on Semiconductor Parameters*, 1 ed. London: World Scientific, 1999.
- [35] T. A. Fjeldly and M. S. Shur, "Simulation and modeling of compound semiconductor devices," *International Journal of High Speed Electronics and Systems*, vol. 6, no. 01, pp. 237-284, 1995.
- [36] W. Knap, V. Kachorovskii, Y. Deng, S. Rumyantsev, J. Q. Lü, R. Gaska, M. S. Shur, G. Simin, X. Hu, M. A. Khan, C. A. Saylor, and L. C. Brunel, "Nonresonant detection of terahertz radiation in field effect transistors," *Journal of Applied Physics*, vol. 91, no. 11, pp. 9346-9353, 2002.
- [37] G. W. Ludwig and R. L. Watters, "Drift and Conductivity Mobility in Silicon," *Physical Review*, vol. 101, no. 6, pp. 1699-1701, 1956.
- [38] D. C. Look and J. R. Sizelove, "Predicted Maximum Mobility in Bulk GaN," *Applied Physics Letters*, vol. 79, no. 8, pp. 1133-1135, 2001.
- [39] T. T. Mnatsakanov, M. E. Levinshtein, L. I. Pomortseva, S. N. Yurkov, G. S. Simin, and M. A. Khan, "Carrier mobility model for GaN," *Solid-State Electronics*, vol. 47, pp. 111-115, 2003.
- [40] A. Shchepetov, C. Gardès, Y. Roelens, A. Cappy, S. Bollaert, S. Boubanga-Tombet, F. Teppe, D. Coquillat, S. Nadar, N. Dyakonova, H. Videlier, W. Knap, D. Seliuta, R. Vadoklis, and G. Valušis, "Oblique modes effect on terahertz plasma wave resonant detection in InGaAs / InAlAs multichannel transistors," *Applied Physics Letters*, vol. 92, no. 24, p. 242105, 2008.
- [41] T. George, A. K. Dutta, M. S. Islam, M. Shur, G. Rupper, and S. Rudin, "Ultimate limits for highest modulation frequency and shortest response time of field effect transistor," in *Proceedings of SPIE*, 2017, vol. 10194, pp. 1-5.
- [42] C. W. Berrya and M. Jarrahi, "Ultrafast Photoconductors based on Plasmonic Gratings," presented at the International Conference on Infrared, Millimeter, and Terahertz Waves, Houston, TX, USA, 2011.
- [43] M. Shur, S. Rudin, G. Rupper, M. Yamaguchi, X. Shen, and A. Muraviev, "Subpicosecond nonlinear plasmonic response probed by femtosecond optical pulses," presented at the 9th Workshop on Frontiers in Electronics San Juan, Puerto-Rico, 2017.